

On the phase-field algorithm for distinguishing connected regions in digital model

Sijing Lai^a, Bing Jiang^a, Qing Xia^a, Binhu Xia^b, Junseok Kim^c, Yibao Li^{a,*}

^a School of Mathematics and Statistics, Xi'an Jiaotong University, Xi'an 710049, China

^b School of Computer Science, Xijing University, Xi'an 710123, China

^c Department of Mathematics, Korea University, Seoul 02841, Republic of Korea

ARTICLE INFO

Keywords:

Phase field method
Allen–Cahn equation
Connected region
3D reconstruction

ABSTRACT

In this paper, we propose a novel model for the discrimination of complex three-dimensional connected regions. The modified model is grounded on the Allen–Cahn equation. The modified equation not only maintains the original interface dynamics, but also avoids the unbounded diffusion behavior of the original Allen–Cahn equation. This advantage enables us to accurately populate and extract the complex connectivity region of the target part. The model is discretized employing a semi-implicit Crank–Nicolson scheme, ensuring second-order accuracy in both time and space. This paper provides a rigorous proof of the unconditional energy stability of our method, thereby affirming the numerical stability and the physical rationality of the solution. We validate the discriminative ability of the proposed model for 3D complex connected regions.

1. Introduction

As automation and intelligence continue to advance in modern industrial design and manufacturing, the task of extracting internal features from complex systems becomes increasingly vital and challenging. This process is critical for analyzing mechanical flow channels [1], segmenting biomedical images [2], and identifying defects in non-destructive testing [3]. The shape of the internal cooling cavity significantly influences airflow performance and blades longevity [4]. In thermal fluid analysis, accurately identifying connected regions within blades cooling cavities is crucial [5]. This process is analogous to medical imaging, where delineating connected organ shapes via Computed Tomography (CT) or Magnetic Resonance Imaging is vital for diagnosis [6,7].

To address these challenges more effectively, certain commercial Computer-Aided Design software integrates specialized modules for extracting connected regions. These modules utilize either mesh-based or voxel-based algorithms to spatially partition the target entity model and identify internal voids by analyzing connected elements. However, their efficacy remains confined to topologically simple flow regions. When confronted with highly complex industrial components, traditional algorithms encounter difficulties due to the exponential growth in meshing precision and data scale. Zhu et al. [8] applied deep learning techniques to semantic segmentation in orbital CT scans. Their approach accurately measured extraocular muscle and optic nerve

volumes. However, it is essential to acknowledge that subjective factors and anatomical complexities may influence the results. Lee et al. [9] focused on liver segmentation using a level set method. Their approach achieved precise extraction through seed region growth and shape propagation. Nevertheless, changes in liver morphology and the presence of similar structures pose challenges in liver segmentation. Yang et al. [10] introduced a novel topological graph-based method for skeleton extraction from binary medical images. By preserving topological relationships, their approach enhanced skeletal structure extraction. However, it fell short in handling curved skeletons, which remained an area for further investigation. Bowden et al. [11] explored active contours and the Poisson equation to address connected region issues in medical images. Their method improved boundary detection and reduces noise. However, it come with high computational demands and requires user-dependent parameter tuning. Consequently, these methods encounter significant challenges when addressing complex geometries marked by pronounced curvature and extensive branching. The modeling approach based on the Allen–Cahn (AC) equation has been widely applied in the field of materials science and engineering, encompassing important physical processes and phenomena such as phase transitions [12–14], average curvature motion [15–17], image analysis [18,19], crystal growth [20–22] and fluid flow [23–25]. The AC equation is capable of describing and tracking highly complex interface shapes and topological changes [26,27]. It exhibits good

* Corresponding author.

E-mail address: yibaoli@xjtu.edu.cn (Y. Li).

URL: <http://gr.xjtu.edu.cn/web/yibaoli> (Y. Li).

<https://doi.org/10.1016/j.enganabound.2024.105918>

Received 19 June 2024; Received in revised form 8 August 2024; Accepted 8 August 2024

Available online 13 August 2024

0955-7997/© 2024 Elsevier Ltd. All rights are reserved, including those for text and data mining, AI training, and similar technologies.

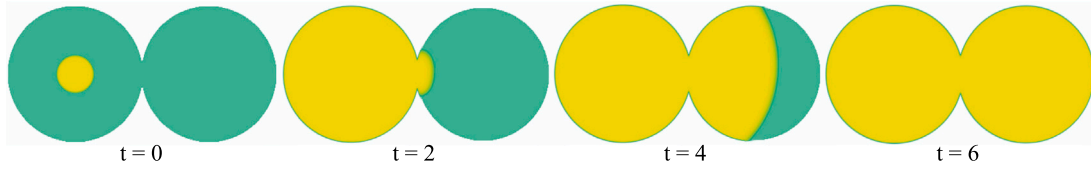


Fig. 1. The diffusion and evolution process of ϕ , initiated from a circular seed, within the Ω_D region of ψ . The green area represents the region within the tangent circle, denoted as Ω_D , and the yellow area illustrates the diffusion evolution of the circular seed within the tangent circle.

stability [28,29] and high accuracy [30,31], making it particularly effective in handling phase interface problems with intricate structures and dynamic variations. Furthermore, it excels in identifying highly curved and complex connected regions.

This study proposes a new model based on the AC equation. This model aims to identify connected regions efficiently through mathematical and physical methodologies. In this study, the modified AC equation preserves the original features of the interface dynamics and avoids the unbounded diffusion of the original equation. This allows for accurate filling and extraction of complex connected regions in the target component. The model is discretized using a semi-implicit Crank–Nicolson scheme, ensuring second-order accuracy in both time and space. This paper rigorously proves the unconditional energy stability of the phase-field model. This model effortlessly manages complex 3D shapes, delivering both high-speed computation and stable results.

The paper is organized as follows: Section 2 describes the governing equations and numerical solution algorithms. Section 3 presents numerical schemes. Section 4 conducts various numerical experiments. Finally, Section 5 provides a conclusion.

2. Methodology

We define the discrete function $\psi(\mathbf{x})$ to represent the areas inside and outside the surface of a three-dimensional model within the region $\Omega = (0, L_x) \times (0, L_y) \times (0, L_z) \subset \mathbb{R}^3$, where $\mathbf{x} = (x, y, z) \in \Omega$. Assuming that the phase field function $\phi(\mathbf{x}, t)$ propagates under the influence of mean curvature flow, where the normal velocity of the moving hypersurface is equal to the negative mean curvature, we establish the initial values of the phase field within the surface of the three-dimensional model. The phase field function begins to diffuse from its initial state and stops when it encounters resistance from the surface of the 3D model. This process effectively distinguishes between connected regions and obstructed areas, thereby identifying the connected regions within the model's surface. In this paper, we propose a modified Allen–Cahn equation for identifying connected regions as follows:

$$\frac{\partial \phi}{\partial t} = M \left(\nabla \cdot (\psi \nabla \phi) - \psi \frac{F'(\phi)}{\epsilon^2} \right) \quad \text{with} \quad \psi(\mathbf{x}) = \begin{cases} 1 & \text{if } \mathbf{x} \in \Omega_D, \\ 0 & \text{otherwise.} \end{cases} \quad (1)$$

where M represents the diffusion rate, ϕ is the phase field, ϵ is a parameter related to the interfacial transition layer, Ω_D refers to the region inside the surface of the 3D model, and $F(\phi) = \phi^2(\phi - 1)^2/4$ is a double-well potential. We briefly describe the fundamental mechanisms of the proposed model within the two-dimensional domain $\Omega = [-1, 1] \times [-1, 1]$. Let $\psi(x, y)$ be a discrete function representing the surfaces of two tangent circles, with centers at $(0.3, 0.5)$ and $(-0.3, 0.5)$ and radii of 0.3, respectively. Ω_D represents the region inside the surfaces of these tangent circles. $\phi(x, y, 0)$ represents a circular seed inside one of the tangent circles.

As shown in Fig. 1, the green area represents the region Ω_D inside the tangent circles, while the yellow area demonstrates the evolution process of circular seeds spreading and filling Ω_D inside the tangent circles. The fundamental principles of the proposed phase field model can be summarized as follows: Due to the diffusion effect of the Allen–Cahn equation [32,33], ϕ diffuses within the connected region Ω_D inside the tangent circles. When ϕ reaches the circular boundary, the constraints imposed by $\psi(x, y)$ cause the diffusion to encounter

resistance and cease, ultimately filling the entire region of the tangent circles without spilling over the boundary.

The Allen–Cahn equation describes a geometric evolution law [34, 35], asserting that the normal velocity of an evolving hypersurface is directly proportional to the negative of its mean curvature:

$$V_n = -M\kappa. \quad (2)$$

Here, V_n represents the normal velocity of the geometry, and κ denotes the mean curvature of the surface. The flow ceases when the mean curvature of the volume reaches zero, indicating a smooth boundary and identifying the connected regions within the entire domain. We can also obtain Eq. (1) by applying the L^2 gradient flow of the Lyapunov energy functional:

$$F = \int_{\Omega} M\psi \left(\frac{1}{2} |\nabla \phi|^2 + \frac{F(\phi)}{\epsilon^2} \right) d\mathbf{x}. \quad (3)$$

By calculating the variational derivative of Eq. (3) using the L^2 norm, we derive Eq. (1) as $\partial \phi / \partial t = -\delta F / \delta \phi$. Additionally, differentiating the total energy F yields

$$\frac{dF}{dt} = \int_{\Omega} \frac{\delta F}{\delta \phi} \frac{\partial \phi}{\partial t} d\mathbf{x} = \int_{\Omega} \left(-\frac{\partial \phi}{\partial t} \right) \frac{\partial \phi}{\partial t} d\mathbf{x} = - \int_{\Omega} \left(\frac{\partial \phi}{\partial t} \right)^2 d\mathbf{x} \leq 0, \quad (4)$$

which indicates a reduction in the total energy as a function of time.

To effectively handle the nonlinear terms in the energy functional and achieve a fully decoupled linear system. Let us define the auxiliary variable $\eta(t)$, and rewrite the system (1) as the following equivalent system:

$$\frac{\partial \phi}{\partial t} = M \left(\nabla \cdot (\psi \nabla \phi) - \psi \eta(t) \frac{F'(\phi)}{\epsilon^2} \right), \quad (5a)$$

$$\frac{d}{dt} \int_{\Omega} F(\phi) d\mathbf{x} = \eta(t) \int_{\Omega} F'(\phi) \frac{\partial \phi}{\partial t} d\mathbf{x}. \quad (5b)$$

with the Neumann boundaries conditions $\mathbf{n} \cdot \nabla \phi = 0$. By assigning the initial condition of $\eta(t)$ as $\eta(0) = 1$, it becomes apparent that the new system (5) corresponds to the original system (1), implying that $\eta(t) = 1$ remains valid in Eq. (5).

Remark 1. We modified the classic Allen–Cahn equation to facilitate the identification of connected regions in complex models. Both the Allen–Cahn and Cahn–Hilliard (CH) equations incorporate mean curvature effects, they fundamentally differ in their properties, particularly regarding mass conservation. This distinction significantly influences their applicability in identifying connected regions. The AC equation is notably characterized by its lack of mass conservation. This non-conserving nature allows the total mass of the system to change during evolution. In the context of identifying connected regions, this characteristic enables interfaces to freely expand throughout the computational domain, unrestricted by the initial mass distribution. Such flexibility allows the AC equation to more effectively explore the entire domain, facilitating the discovery and identification of potential connected regions within the entire area. In contrast, the CH equation is distinguished by its strict mass conservation property [36–38]. This conservativeness arises from the inclusion of a squared Laplacian term in the CH equation, ensuring that the total mass of the system remains constant over time. When applied to the identification of connected regions, this mass conservation means that interface movement is heavily constrained by the initial mass distribution, limiting its ability to explore the entire computational domain.

3. Discrete schemes and energy dissipation

Let us introduce the discrete operators and formulation with the second-order central difference method. The discrete system is illustrated by considering the 3D domain $\Omega_p^d = [0, L_x] \times [0, L_y] \times [0, L_z]$. We discretize the computational domain with a uniform mesh grid, whose mesh size is computed as $h = L_x/N_x = L_y/N_y = L_z/N_z$ with the positive even integers N_x, N_y and N_z on the x -, y - and z -directions, respectively. Let us denote i, j and k as the directional index, thus we can define $\phi_{i,j,k}^n$ as the approximation to $\phi(x_i, y_j, z_k, n\Delta t)$, where $x_i = (i - 0.5)h$, $y_j = (j - 0.5)h$, $z_k = (k - 0.5)h$, $\Delta t = T/N$, T is the final time, and N is the total time step. Therefore, the cell vertices can be denoted as $(x_{i+\frac{1}{2}}, y_{j+\frac{1}{2}}) := (ih, jh)$. Let us define the discrete gradient operator as

$$\nabla_d \phi_{i,j,k} = \left(D_x \phi_{i+\frac{1}{2},j,k}, D_y \phi_{i,j+\frac{1}{2},k}, D_z \phi_{i,j,k+\frac{1}{2}} \right), \quad (6)$$

where $D_x \phi_{i+\frac{1}{2},j,k} = (\phi_{i+1,j,k} - \phi_{i,j,k})/h$, $D_y \phi_{i,j+\frac{1}{2},k} = (\phi_{i,j+1,k} - \phi_{i,j,k})/h$ and $D_z \phi_{i,j,k+\frac{1}{2}} = (\phi_{i,j,k+1} - \phi_{i,j,k})/h$. Furthermore, we define the discrete inner products and discrete norms as:

$$(\phi, \psi)_d = h^3 \sum_{i=1}^{N_x} \sum_{j=1}^{N_y} \sum_{k=1}^{N_z} \phi_{i,j,k} \psi_{i,j,k}, \quad (7)$$

$$(\nabla_d \phi, \nabla_d \psi)_d = h^3 \sum_{i=1}^{N_x} \sum_{j=1}^{N_y} \sum_{k=1}^{N_z} \left(D_x \phi_{i+\frac{1}{2},j,k} D_x \psi_{i+\frac{1}{2},j,k} + D_y \phi_{i,j+\frac{1}{2},k} D_y \psi_{i,j+\frac{1}{2},k} + D_z \phi_{i,j,k+\frac{1}{2}} D_z \psi_{i,j,k+\frac{1}{2}} \right), \quad (8)$$

$$\|\phi\|_d^2 = (\phi, \phi)_d, \quad \|\nabla_d \phi\|_d^2 = (\nabla_d \phi, \nabla_d \phi)_d. \quad (9)$$

We develop the following numerical scheme based on the Crank–Nicolson temporal discretization:

$$\frac{\phi^{n+1} - \phi^n}{\Delta t} = M \left(\nabla_d \cdot (\psi \nabla_d \phi^{n+\frac{1}{2}}) - \psi \eta^{n+\frac{1}{2}} \frac{F'(\hat{\phi}^{n+\frac{1}{2}})}{\epsilon^2} \right), \quad (10a)$$

$$\left(F(\phi^{n+1}) - F(\phi^n), 1 \right)_d = \eta^{n+\frac{1}{2}} \left(F'(\hat{\phi}^{n+\frac{1}{2}}), \phi^{n+1} - \phi^n \right)_d, \quad (10b)$$

with the Neumann boundaries conditions $\nabla_d \phi^{n+1} \cdot \mathbf{n}|_{\partial\Omega} = 0$. Here, we denote $\phi^{n+\frac{1}{2}} = (\phi^{n+1} + \phi^n)/2$, $\hat{\phi}^{n+\frac{1}{2}} = (3\phi^n - \phi^{n-1})/2$. We consider $\nabla_d \cdot (\psi \nabla_d \phi^{n+\frac{1}{2}})$ as

$$\begin{aligned} \nabla_d \cdot (\psi \nabla_d \phi^{n+\frac{1}{2}})_{i,j,k} &= \frac{1}{h^2} \left(\psi_{i+\frac{1}{2},j,k} (\phi_{i+1,j,k}^{n+\frac{1}{2}} - \phi_{i,j,k}^{n+\frac{1}{2}}) - \psi_{i-\frac{1}{2},j,k} (\phi_{i,j,k}^{n+\frac{1}{2}} - \phi_{i-1,j,k}^{n+\frac{1}{2}}) \right) \\ &+ \frac{1}{h^2} \left(\psi_{i,j+\frac{1}{2},k} (\phi_{i,j+1,k}^{n+\frac{1}{2}} - \phi_{i,j,k}^{n+\frac{1}{2}}) - \psi_{i,j-\frac{1}{2},k} (\phi_{i,j,k}^{n+\frac{1}{2}} - \phi_{i,j-1,k}^{n+\frac{1}{2}}) \right) \\ &+ \frac{1}{h^2} \left(\psi_{i,j,k+\frac{1}{2}} (\phi_{i,j,k+1}^{n+\frac{1}{2}} - \phi_{i,j,k}^{n+\frac{1}{2}}) - \psi_{i,j,k-\frac{1}{2}} (\phi_{i,j,k}^{n+\frac{1}{2}} - \phi_{i,j,k-1}^{n+\frac{1}{2}}) \right). \end{aligned} \quad (11)$$

We employ the Picard iteration method to solve Eq. (10a), updating $\eta^{n+\frac{1}{2}}$ and ϕ^{n+1} as follows:

$$\frac{\phi^{n+1,m+1} - \phi^n}{\Delta t} = M \nabla_d \cdot (\psi \nabla_d \phi^{n+\frac{1}{2},m}) - M \eta^{n+\frac{1}{2}} \frac{\psi}{\epsilon^2} F'(\hat{\phi}^{n+\frac{1}{2}}), \quad (12a)$$

$$\left(F(\phi^{n+1,m}) - F(\phi^n), 1 \right)_d = \eta^{n+\frac{1}{2}} \left(F'(\hat{\phi}^{n+\frac{1}{2}}), \phi^{n+1,m} - \phi^n \right)_d, \quad (12b)$$

where $\phi^{n+\frac{1}{2},m} = (\phi^n + \phi^{n+1,m})/2$, m is the index of Picard iteration. The initial condition are chosen as $\phi^{n+1,0} = 2\phi^n - \phi^{n-1}$, $\eta^0 = 1$. The computation is performed until the error is smaller than a given tolerance as

$$\|\phi^{n+1,m+1} - \phi^{n+1,m}\|_d^2 < tol. \quad (13)$$

Then we set $\phi^{n+1} = \phi^{n+1,m+1}$, obtaining the updated ϕ^{n+1} . It should be pointed out that our purpose is to find the approximate solutions around $\eta^{n+\frac{1}{2}} = 1$, which is simple with lower computation cost if we use $\eta^0 = 1$ as the initial condition.

Herein, we can drive the unconditional energy stability of the numerical scheme Eq. (10) as follows.

Theorem 1. The CN schemes (10) are unconditionally energy stable satisfying the following discrete energy dissipation law

$$\begin{aligned} \frac{E^{n+1} - E^n}{\Delta t} &= - \left\| \frac{\phi^{n+1} - \phi^n}{\Delta t} \right\|_d^2 \leq 0 \quad \text{with} \\ E^n &= \frac{M}{2} \left(\psi, \|\nabla_d \phi^n\|_d^2 \right)_d + \frac{M}{\epsilon^2} \left(\psi, F(\phi^n) \right)_d. \end{aligned} \quad (14)$$

Proof. Let us take the L_2 inner product of Eq. (10a) with $(\phi^{n+1} - \phi^n)/\Delta t$ as follows:

$$\begin{aligned} \left\| \frac{\phi^{n+1} - \phi^n}{\Delta t} \right\|_d^2 &= - \frac{M}{2} \left(\psi, \|\nabla_d \phi^{n+1}\|_d^2 - \|\nabla_d \phi^n\|_d^2 \right)_d \\ &- \frac{M}{\epsilon^2} \left(\psi, F(\phi^{n+1}) - F(\phi^n) \right)_d. \end{aligned} \quad (15)$$

Thus, we have the following energy dissipation law:

$$\begin{aligned} \frac{E^{n+1} - E^n}{\Delta t} &= \frac{M}{2} \left(\psi, \|\nabla_d \phi^{n+1}\|_d^2 \right)_d + \frac{M}{\epsilon^2} \left(\psi, F(\phi^{n+1}) \right)_d - \frac{M}{2} \left(\psi, \|\nabla_d \phi^n\|_d^2 \right)_d \\ &- \frac{M}{\epsilon^2} \left(\psi, F(\phi^n) \right)_d \\ &= \frac{M}{2} \left(\psi, \|\nabla_d \phi^{n+1}\|_d^2 - \|\nabla_d \phi^n\|_d^2 \right)_d + \frac{M}{\epsilon^2} \left(\psi, F(\phi^{n+1}) - F(\phi^n) \right)_d \\ &= - \left\| \frac{\phi^{n+1} - \phi^n}{\Delta t} \right\|_d^2 \leq 0. \end{aligned}$$

This completes the proof.

Remark 2. Our developed model (10) employs the central difference scheme for spatial discretization and the Crank–Nicolson scheme for time integration. The central difference scheme is renowned for its second-order accuracy in space, as it approximates derivatives using the average rate of change between adjacent grid points. This method minimizes truncation errors, ensuring a high level of accuracy in spatial discretization. For time discretization, the Crank–Nicolson scheme is adopted, which results in the trapezoidal rule for integration, achieving second-order accuracy in time. Our discretization of the model is based on the Lagrange multiplier method, employing the semi-implicit Crank–Nicolson scheme and central difference, thus endowing our scheme with second-order accuracy.

4. Numerical experiments

In this section, we perform several numerical simulations in two- and three-dimensional domains. Unless otherwise specified, we choose Neumann boundary conditions for the numerical simulations. The parameter settings were as follows: $\epsilon = 6h/(2\sqrt{2}\tanh(0.9))$, $M = 1$, and $\Delta t = 0.1h$.

4.1. Numerical stability

In this section, we numerically check the energy dissipation and stability of the proposed system at four different time steps. The initial conditions are set as follows:

$$\phi(x, y, 0) = 0.75 - 0.25 \tanh \left(\frac{\sqrt{(x-0.3)^2 + (y-0.5)^2} - 0.1}{\sqrt{2}\epsilon} \right), \quad (16)$$

$$\psi(x, y) = \begin{cases} 1 & \text{if } (x, y) \in \Omega_D, \\ 0 & \text{otherwise.} \end{cases} \quad (17)$$

Here, $\psi(x, y)$ represents the discrete surface function of two tangent circles with centers at (0.3, 0.5) and (0.7, 0.5), both having a radius of 0.2. The region Ω_D denotes the area enclosed by this surface. As shown in Fig. 2, we compare the evolution of the total energy at different time steps $\Delta t = 10, 1, 0.1$, and 0.01 over time until $T = 100$. The consistent decline observed in all four energy curves signifies a robust numerical solution. This affirms compliance of the system with energy

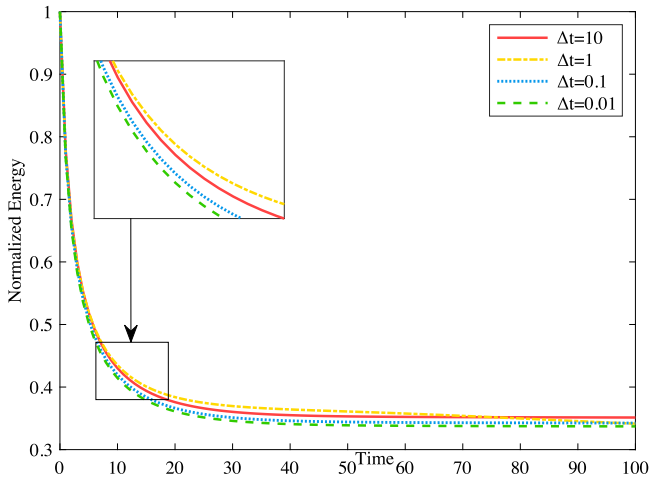


Fig. 2. Curve graph of the normalized energy functional evolving over time with four different time steps $\Delta t = 10, 1, 0.1$, and 0.01 . The subgraph is local curve enlargements at the turning points.

dissipation laws and facilitates the application of larger investigative time steps. Additionally, Fig. 2 includes a magnified subplot that clearly displays the differences in the curves at the turning points. Clearly, the curve obtained with $\Delta t = 0.1$ aligns closely with the one obtained with $\Delta t = 0.01$. However, when larger time steps are chosen, such as $\Delta t = 10$ and $\Delta t = 1$, the energy curves differ more significantly. Although the difference is not very noticeable for large states, it is recommended to use smaller time steps to obtain more accurate numerical solutions. We can easily conclude that our numerical solutions are convergent, and the proposed scheme shows effectiveness even for large time steps. Therefore, to maintain the accuracy of our proposed scheme while reducing computational costs, an appropriate value for Δt is $\Delta t = 0.1$.

4.2. Convergence test

In this section, we present two numerical experiments to validate the convergence of our second-order numerical schemes in both space and time. The initial conditions are set as follows:

$$\phi(x, y, 0) = 0.75 - 0.25 \tanh\left(\frac{\sqrt{(|x| - 0.3)^2 + (y - 0.5)^2} - 0.1}{\sqrt{2}\epsilon}\right), \quad (18)$$

$$\psi(x, y) = \begin{cases} 1 & \text{if } (x, y) \in \Omega_D, \\ 0 & \text{otherwise.} \end{cases} \quad (19)$$

Here, $\psi(x, y)$ represents the discrete surface function of two tangent circles with centers at $(0.3, 0.5)$ and $(0.7, 0.5)$, both having a radius of 0.2 , where Ω_D denotes the area enclosed by this surface. Since an analytic solution is unavailable, we derive a reference solution denoted as ϕ^{ref} using extremely fine temporal steps and grid sizes. For temporal convergence assessment, we employ a sequence of diminishing time steps: $\Delta t = 1, 0.5, 0.25$, and 0.125 , respectively. The spatial dimension remains fixed at $h = 1/256$. The reference solution is computed with a fine time step of $\Delta t = 0.0625$. We define the error as $e_{i,\Delta t} = \phi_{i,\Delta t} - \phi_i^{ref}$, and the convergence rate is expressed as $\log_2(\|e_{i,\Delta t}\|_2 / \|e_{i,\Delta t/2}\|_2)$. These results are summarized in Table 1, confirming the second-order time accuracy of our scheme. For spatial convergence analysis, we maintain a fixed temporal step size of $\Delta t = 0.1$ and systematically decrease the spatial step sizes: $h = 1/32, 1/64, 1/128$, and $1/256$, respectively. The reference solution corresponds to a very fine spatial mesh with $h = 1/512$. The grid error is defined as $e_{i,h} = \phi_{i,h} - \phi_i^{ref}$, and the convergence rate is calculated as $\log_2(\|e_{i,h}\|_2 / \|e_{i,h/2}\|_2)$. These results are presented in Table 2, demonstrating the second-order spatial accuracy of our scheme.

Table 1

Numerical error and convergence rate by using different time steps for the phase field variable ϕ .

Δt	1	0.5	0.25	0.125
l_2 error	1.600e-2	3.800e-3	9.646e-4	2.575e-4
Rate		2.06	1.99	1.91

Table 2

Numerical error and convergence rate by using different spacial steps for the phase field variable ϕ .

h	1	0.5	0.25	0.125
l_2 error	1.090e-2	2.700e-3	6.708e-4	1.648e-4
Rate		2.00	2.01	2.02

4.3. Comparison and verification of various numerical methods

In this section, we employ the Invariant Energy Quadratzation (IEQ) method, the Scalar Auxiliary Variable (SAV) method, and the proposed Lagrange multiplier method to study and compare their effectiveness. The IEQ method requires solving linear equations with complex variable coefficients and imposes constraints on the boundedness of the free energy density. The SAV method [39,40] improves upon the IEQ method [41] by relaxing the requirements on the energy density function. However, it still demands that the integral of the nonlinear functional in the free energy be bounded from below. It is noteworthy that both the SAV and IEQ methods operate on modified energy rather than the original energy. The Lagrange multiplier method inherits most of the advantages of the SAV and IEQ methods while avoiding the boundedness requirement of the energy density functional. We first present the discrete system established based on the IEQ method as follows:

$$\frac{\phi^{n+1} - \phi^n}{\Delta t} = M \left(\nabla_d \cdot (\psi \nabla_d \phi^{n+\frac{1}{2}}) - \frac{\psi F'(\hat{\phi}^{n+\frac{1}{2}})}{\epsilon^2 \sqrt{F(\phi^{n+\frac{1}{2}}) + B_{IEQ}}} u^{n+\frac{1}{2}} \right), \quad (20a)$$

$$\frac{u^{n+1} - u^n}{\Delta t} = \frac{F'(\hat{\phi}^{n+\frac{1}{2}})(\phi^{n+1} - \phi^n)}{2\Delta t \sqrt{F(\phi^{n+\frac{1}{2}}) + B_{IEQ}}}. \quad (20b)$$

Here, $u(t, \phi) = \sqrt{F(\phi) + B_{IEQ}}$ is the auxiliary variable, where B_{IEQ} is a positive constant that ensures $B_{IEQ} > -F(\phi)$. The discrete system established based on the SAV method is given as:

$$\frac{\phi^{n+1} - \phi^n}{\Delta t} = M \left(\nabla_d \cdot (\psi \nabla_d \phi^{n+\frac{1}{2}}) - \frac{\psi F'(\hat{\phi}^{n+\frac{1}{2}})}{\epsilon^2 \sqrt{\int_{\Omega} F(\phi^{n+\frac{1}{2}}) d\mathbf{x} + B_{SAV}}} v^{n+\frac{1}{2}} \right), \quad (21a)$$

$$\frac{v^{n+1} - v^n}{\Delta t} = \frac{\int_{\Omega} F'(\hat{\phi}^{n+\frac{1}{2}})(\phi^{n+1} - \phi^n) d\mathbf{x}}{2\Delta t \sqrt{\int_{\Omega} F(\phi^{n+\frac{1}{2}}) d\mathbf{x} + B_{SAV}}}. \quad (21b)$$

Here, $v(t) = \sqrt{\int_{\Omega} F(\phi) d\mathbf{x} + B_{SAV}}$ is the auxiliary variable, where B_{SAV} is a positive constant that satisfies $B_{SAV} > -\int_{\Omega} F(\phi) d\mathbf{x}$.

To conduct a rigorous comparative analysis of the effectiveness of these three numerical algorithms, we performed instantiated simulations under the same initial conditions:

$$\phi(x, y, 0) = 0.75 - 0.25 \tanh\left(\frac{|x - 0.16| + |x - 0.36| + |y - 0.4| + |y - 0.6| - 0.49}{2\sqrt{2}\epsilon}\right), \quad (22)$$

$$\psi(x, y) = \begin{cases} 1 & \text{if } (x, y) \in \Omega_D, \\ 0 & \text{otherwise.} \end{cases} \quad (23)$$

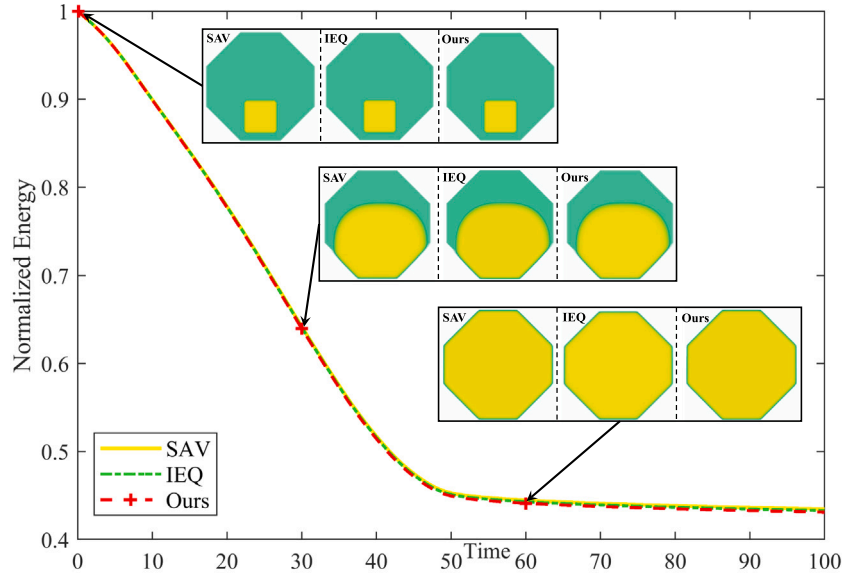


Fig. 3. Comparison of the normalized energy dissipation curves and the evolution of the phase field variable under the same initial conditions for the SAV, IEQ, and our Lagrange multiplier methods. The three rows of subfigures, from top to bottom, respectively show the evolution of the phase field variable ϕ at times $T = 0$, $T = 30$, and $T = 60$ for the three numerical methods. In each subfigure, the three smaller plots from left to right correspond to the SAV, IEQ, and our method, respectively.

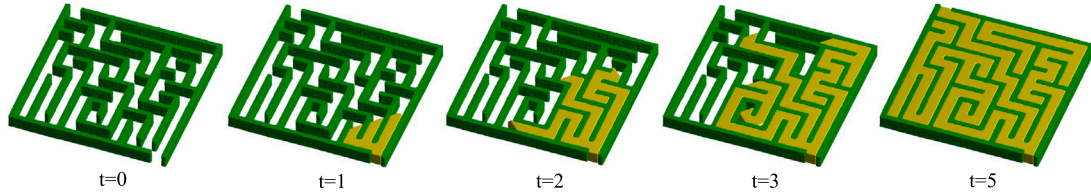


Fig. 4. The evolution process of distinguishing connected regions on the surface of the maze model. The green represents the maze model, and the yellow shows the evolution process of ϕ diffusing and filling Ω_D on the surface of the maze model.

Here, $\psi(x, y)$ denotes the discrete surface function of an octagon, where Ω_D represents the region within that surface. This is done to determine the energy stability during diffusion. As illustrated in Fig. 3, the normalized energy dissipation characteristics of three numerical methods under identical conditions are displayed. The three rows of subfigures in Fig. 3 show the evolution of the phase field variable ϕ at moments $T = 0$, $T = 30$, and $T = 60$ for SAV, IEQ, and our method, respectively. It can be observed that there are no significant differences in the evolution of the phase field variable ϕ among the three numerical methods. Moreover, the numerical evolution curves shown in Fig. 3 indicate that the energy dissipation trends are consistent across the three methods, with no significant differences. However, the energy dissipation obtained by our Lagrange multiplier method tends to stabilize more quickly. It is imperative to acknowledge that the incorporation of auxiliary variables in the SAV and IEQ methods necessitates the establishment of a lower bound for the free energy functional integral, thereby endowing the auxiliary structure with effectiveness. In contrast, when applying the Lagrange multiplier method, the objective of the solution is to find an approximate solution near $\eta^{n+\frac{1}{2}} = 1$. If we use $\eta^0 = 1$ as the initial condition, a rapid and efficient solution can be achieved.

4.4. Evolution of distinguishing connected regions

In this section, we simulate the visually distinguishable evolution process of connected regions within a grass maze within the domain $\Omega = [0, 1] \times [0, 1] \times [0, 1]$. Let $\psi(x, y, z)$ be a discrete function composed of point set data from the three-dimensional maze, and Ω_D be the region inside the maze boundary. We set an initial seed ϕ at the

entrance of the maze. Due to the diffusion effect of the AC equation, ϕ grows by diffusion in the region Ω_D on the surface of the maze model. However, the growth is constrained by $\psi(x, y, z)$, causing ϕ to encounter resistance upon reaching the boundary of the maze surface. This halts the diffusion growth, leading to the eventual filling of all connected regions within the maze surface. As shown in Fig. 4, the green represents the maze model, and the yellow shows the diffusion growth of ϕ on the surface of the maze model, thereby filling Ω_D in the evolution process. This demonstrates that our method can effectively discern a complete and smooth connected region.

4.5. Point cloud reconstruction of a target model

In this section, we consider a sphere with center $(0.4, 0.4, 0.4)$ and radius 0.2 within the domain $\Omega = [0, 1] \times [0, 1] \times [0, 1]$ as the initial value $\phi(x, y, z, 0)$ of the phase field. The point cloud data on a three-dimensional Stanford bunny model serves as the discrete function $\psi(x, y, z)$, and Ω_D represents the region inside the surface of the three-dimensional Stanford bunny model:

$$\phi(x, y, z, 0) = 0.75 - 0.25 \tanh\left(\frac{\sqrt{(x-0.4)^2 + (y-0.4)^2 + (z-0.4)^2} - 0.2}{\sqrt{2}\epsilon}\right), \quad (24)$$

$$\psi(x, y, z) = \begin{cases} 1 & \text{if } (x, y, z) \in \Omega_D, \\ 0 & \text{otherwise.} \end{cases} \quad (25)$$

As shown in Fig. 5, the evolution of the phase field function ϕ from the initial sphere to the three-dimensional Stanford bunny model is displayed. The green area represents the target Stanford bunny model, while the yellow area illustrates the diffusion growth of the phase field

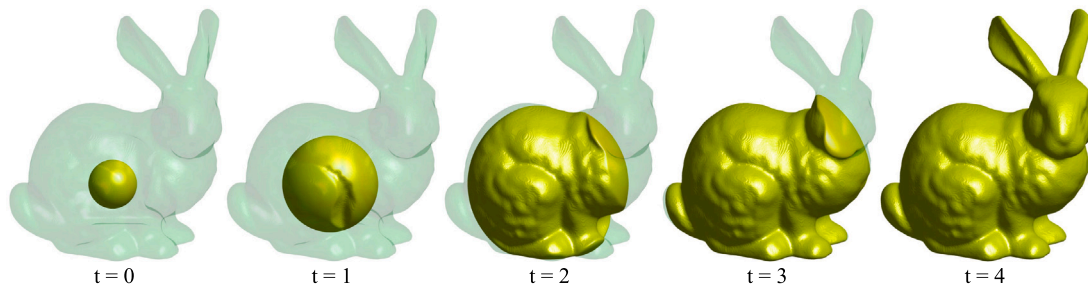


Fig. 5. The phase field function ϕ grows outward from an initial sphere, reconstructing the evolution process of the three-dimensional Stanford bunny model.

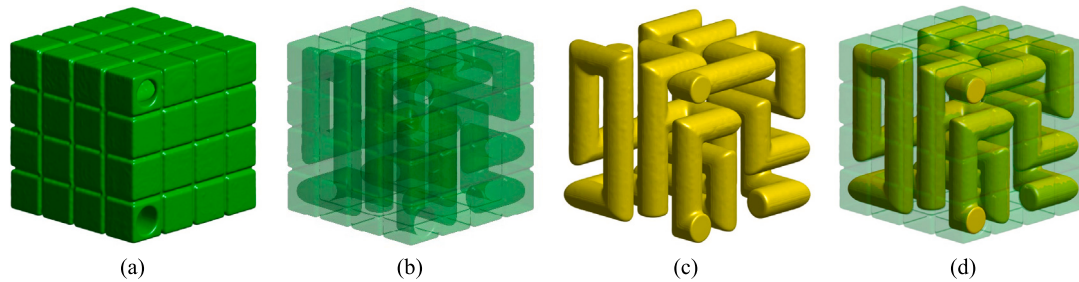


Fig. 6. (a) represents the schematic of the surface of the cube model, (b) is the internal perspective view of the cube model, (c) is the connected region within the surface extracted from the experiment, and (d) is the matching diagram of the extracted connected region within the surface and the internal connecting channels of the cube model: yellow area represents the experimentally extracted internal connected region, and green area represents the cube model.

ϕ within Ω_D starting from the initial sphere until it fills the entire Stanford bunny model. Due to the diffusion effect of the Allen–Cahn equation, the phase field function ϕ diffuses and grows outward from the initial spherical state within the surface of the Stanford bunny model. Upon reaching the surface of the Stanford bunny model, it encounters resistance and halts its diffusion. Consequently, it fills the region within the surface of the model, thereby accomplishing the reconstruction of the Stanford bunny model from the point cloud.

4.6. Discrimination of invisible complex connected regions inside objects

In this section, we consider a complex three-dimensional Cube maze model, which does not allow the interior to be seen from the surface, as shown in Fig. 6(a) and (b). An initial seed $\phi(x, y, z, 0)$ is placed at the entrance of the maze, and the point cloud data on the three-dimensional Cube model is treated as a discrete function $\psi(x, y, z)$. Due to the diffusion effect of the AC equation and the regional constraints of $\psi(x, y, z)$, ϕ spreads and grows within the surface area of the Cube model. This diffusion continues until it encounters an obstruction at the surface of the model, eventually filling the connected region within the model surface. Consequently, we can effectively discern the connected regions inside the Cube. As illustrated in Fig. 6(c), by identifying the connected regions within the surface, we have determined the pathways of the Cube maze. Fig. 6(d) presents a comparison between the connected regions extracted from the experiment and the internal conduits of the Cube model: the yellow area represents the experimentally extracted internal connected regions, and the green area represents the Cube model. It is evident from Fig. 6(d) that the connected regions extracted from the surface of the Cube correspond precisely with the internal conduits of the model, indicating that our method can successfully identify complete and smooth connected regions.

5. Conclusion

In this paper, a novel model based on phase field theory was proposed to efficiently and accurately discriminate complex three-dimensional connected regions. The proposed phase-field model was

based on the AC equation, which is a partial differential equation describing the dynamics of interfaces. The diffusion term in the AC equation facilitates changes within the phase field inside the material, forming a diffusive interface, thereby achieving the separation of phases. Our improved AC equation not only maintained the original interface dynamics, but also avoided the unbounded diffusion behavior of the original AC equation, which enabled us to accurately populate and extract the complex connectivity region of the target part. The model was discretized employing the semi-implicit Crank–Nicolson scheme, which guarantees second-order accuracy. This approach is crucial for ensuring the unconditional energy stability of the model, thereby maintaining the physical integrity of the numerical stability and solution.

CRediT authorship contribution statement

Sijing Lai: Writing – original draft, Visualization, Software, Methodology, Investigation, Formal analysis, Data curation, Conceptualization. **Bing Jiang:** Writing – original draft, Methodology, Formal analysis, Conceptualization. **Qing Xia:** Writing – original draft, Methodology, Formal analysis, Conceptualization. **Binhu Xia:** Writing – review & editing, Visualization, Investigation, Conceptualization. **Junseok Kim:** Writing – review & editing, Supervision, Investigation, Conceptualization. **Yibao Li:** Writing – review & editing, Supervision, Methodology, Funding acquisition, Conceptualization.

Declaration of competing interest

The authors declare that they have no known competing financial interests or personal relationships that could have appeared to influence the work reported in this paper.

Data availability

No data was used for the research described in the article.

Acknowledgments

This work is supported by Natural Science Basic Research Program of Shaanxi (Program No. 2024JC-YBMS-016, 2024JC-YBMS-068) and Shaanxi Fundamental Science Research Project for Mathematics and Physics (Grant No. 23JSQ054). The authors are grateful to the reviewers whose valuable suggestions and comments significantly improved the quality of this paper.

References

- [1] Dai H, Zhang J, Ren Y, Liu N, Lin J. Effect of cooling hole configurations on combustion and heat transfer in an aero-engine combustor. *Appl Therm Eng* 2021;182:115664.
- [2] Fu Y, Lei Y, Wang T, Curran WJ, Liu T, Yang X. A review of deep learning based methods for medical image multi-organ segmentation. *Phys Med* 2021;85:107–22.
- [3] Lu QY, Wong CH. Additive manufacturing process monitoring and control by non-destructive testing techniques: challenges and in-process monitoring. *Virt Phys Prototy* 2018;13(2):39–48.
- [4] Yue Z. The recent progress in the design of structural strength and life assessment for aero-engine single crystal turbine blades. *Mater High Temp* 2024;(1):1–12.
- [5] Li D, Yuan H, Ma S, Yang J. Dynamic coupling analysis on thermo-chemo-mechanical field and fluid-structure interaction for aero-engine turbine blade with functional gradient thermal barrier coatings. *Coatings* 2022;12(10):1498.
- [6] Cerrolaza JJ, Picazo ML, Humbert L, Sato Y, Rueckert D, Ballester MAG, et al. Computational anatomy for multi-organ analysis in medical imaging: A review. *Med Image Anal* 2019;56:44–67.
- [7] Roth HR, Shen C, Oda H, Oda M, Hayashi Y, Misawa K, et al. Deep learning and its application to medical image segmentation. *Med Imaging Technol* 2018;36(2):63–71.
- [8] Zhu F, Gao Z, Zhao C, Zhu Z, Tang J, Liu Y, et al. Semantic segmentation using deep learning to extract total extraocular muscles and optic nerve from orbital computed tomography images. *Optik* 2021;244:167551.
- [9] Lee J, Kim N, Lee H, Seo JB, Won HJ, Shin YM, et al. Efficient liver segmentation using a level-set method with optimal detection of the initial liver boundary from level-set speed images. *Comput Methods Prog Biomed* 2007;88(1):26–38.
- [10] Yang L, Oyen D, Wohlberg B. A novel algorithm for skeleton extraction from images using topological graph analysis. In: *Proc IEEE/CVF conf comput vis pattern recog workshops*. 2019.
- [11] Bowden A, Todorov MD, Sirakov NM. Implementation of the Euler–Lagrange and Poisson equations to extract one connected region. *AIP Conf Proc* 2014;1629(1):400–7.
- [12] Liu H, Cheng A, Wang H, Zhao J. Time-fractional allen–cahn and cahn–hilliard phase-field models and their numerical investigation. *Comput Math Appl* 2018;76(8):1876–92.
- [13] Jiang M, Zhao J. Linear relaxation schemes for the Allen–Cahn-type and Cahn–Hilliard-type phase field models. *Appl Math Lett* 2023;137:108477.
- [14] Song X, Xia Q, Kim J, Li Y. An unconditional energy stable data assimilation scheme for Navier–Stokes–Cahn–Hilliard equations with local discretized observed data. *Comput Math Appl* 2024;164:21–33.
- [15] Yang J, Kang S, Kwak S, Kim J. The allen–cahn equation with a space-dependent mobility and a source term for general motion by mean curvature. *J Comput Sci* 2024;102252.
- [16] Song X, Li Y. An efficient numerical method for reaction–diffusion equation on the general curved surfaces. *Appl Math Lett* 2022;133:108268.
- [17] Xia Q, Zhu J, Yu Q, Kim J, Li Y. Triply periodic minimal surfaces based topology optimization for the hydrodynamic and convective heat transfer. *Commun Nonlinear Sci Numer Simul* 2024;131:107819.
- [18] Wang J, Han Z, Kim J. An efficient and explicit local image inpainting method using the Allen–Cahn equation. *Z Angew Math Phys* 2024;75(2):44.
- [19] Wang J, Xu H, Yang J, Kim J. Fractal feature analysis based on phase transitions of the Allen–Cahn and Cahn–Hilliard equations. *J Comput Sci* 2023;72:102114.
- [20] Liu Z, Li X. Efficient modified stabilized invariant energy quadratization approaches for phase-field crystal equation. *Numer Algorithms* 2020;85(1):107–32.
- [21] Li X, Shen J. Stability and error estimates of the SAV Fourier-spectral method for the phase field crystal equation. *Adv Comput Math* 2020;46:1–20.
- [22] Xia Q, Yang J, Kim J, Li Y. On the phase field based model for the crystalline transition and nucleation within the Lagrange multiplier framework. *J Comput Phys* 2024;113158.
- [23] Yang Y, Wang Y, Xiao X, Feng X. Fast and stable dimension splitting simulations for the hydrodynamically coupled three-component conserved Allen–Cahn phase field model. *Int J Multiph Flow* 2024;104765.
- [24] Wang Y, Xiao X, Feng X. Numerical simulation for the conserved Allen–Cahn phase field model of two-phase incompressible flows by an efficient dimension splitting method. *Commun Nonlinear Sci Numer Simul* 2024;131:107874.
- [25] Li Y, Xia Q, Kang S, Kwak S, Kim J. A practical algorithm for the design of multiple-sized porous scaffolds with triply periodic structures. *Math Comput Simulation* 2024;220:481–95.
- [26] Jeong D, Lee S, Lee D, Shin J, Kim J. Comparison study of numerical methods for solving the Allen–Cahn equation. *Comput Mater Sci* 2016;111:131–6.
- [27] Xie W, Feng J, Xia Q, Kim J, Li Y. Design of the shell-infill structures using a phase field-based topology optimization method. *Comput Methods Appl Mech Engrg* 2024;429:117138.
- [28] Quan C, Wang B. Energy stable L2 schemes for time-fractional phase-field equations. *J Comput Phys* 2022;458:111085.
- [29] Quan C, Tang T, Yang J. How to define dissipation-preserving energy for time-fractional phase-field equations. *CSIAM Trans Appl Math* 2020;1(3):478–90.
- [30] Guan Z, Lowengrub J, Wang C. Convergence analysis for second-order accurate schemes for the periodic nonlocal Allen–Cahn and Cahn–Hilliard equations. *Math Methods Appl Sci* 2017;40(18):6836–63.
- [31] Zhai S, Ye C, Weng Z. A fast and efficient numerical algorithm for fractional Allen–Cahn with precise nonlocal mass conservation. *Appl Math Lett* 2020;103:106190.
- [32] Xia B, Yu R, Song X, Zhang X, Kim J. An efficient data assimilation algorithm using the Allen–Cahn equation. *Eng Anal Bound Elem* 2023;155:511–7.
- [33] Emamjomeh M, Nabati M, Dinmohammadi A. Numerical study of two operator splitting localized radial basis function method for Allen–Cahn problem. *Eng Anal Bound Elem* 2024;163:126–37.
- [34] Cui C, Liu J, Mo Y, Zhai S. An effective operator splitting scheme for two-dimensional conservative nonlocal Allen–Cahn equation. *Appl Math Lett* 2022;130:108016.
- [35] Zamani-Gharaghoshi H, Dehghan M, Abbaszadeh M. Numerical solution of Allen–Cahn model on surfaces via an effective method based on generalized moving least squares (GMLS) approximation and the closest point approach. *Eng Anal Bound Elem* 2023;152:575–81.
- [36] Xia Q, Kim J, Li Y. Modeling and simulation of multi-component immiscible flows based on a modified Cahn–Hilliard equation. *Eur J Mech B Fluids* 2022;95:194–204.
- [37] Jiang B, Xia Q, Kim J, Li Y. Efficient second-order accurate scheme for fluid-surfactant systems on curved surfaces with unconditional energy stability. *Commun Nonlinear Sci Numer Simul* 2024;135:108054.
- [38] Li Y, Zhang L, Xia Q, Yu Q, Kim J. An unconditionally energy-stable second-order time-accurate numerical scheme for the coupled cahn–hilliard system in copolymer/homopolymer mixtures. *Comput Mater Sci* 2021;200:110809.
- [39] Cheng J, Xia Q, Kim J, Li Y. An efficient linear and unconditionally stable numerical scheme for the phase field sintering model. *Commun Nonlinear Sci Numer Simul* 2023;127:107529.
- [40] Lai S, Xia Q, Kim J, Li Y. Phase-field based modeling and simulation for selective laser melting techniques in additive manufacturing. *Commun Nonlinear Sci Numer Simul* 2024;108239.
- [41] Li Y, Qin K, Xia Q, Kim J. A second-order unconditionally stable method for the anisotropic dendritic crystal growth model with an orientation-field. *Appl Numer Math* 2023;184:512–26.